

# Electric monopole transition from the superdeformed band in $^{40}\text{Ca}$

E. Ideguchi (井手口栄治),<sup>1</sup> T. Kibédi,<sup>2</sup> J. T. H. Dowie,<sup>2</sup> T. H. Hoang,<sup>1,3</sup> M. Kumar Raju,<sup>1,3</sup> N. Aoi (青井考),<sup>1</sup> A. J. Mitchell,<sup>2</sup> A. E. Stuchbery,<sup>2</sup> N. Shimizu (清水則孝),<sup>4</sup> Y. Utsuno (宇都野穰),<sup>5,4</sup> A. Akber,<sup>2</sup> L. J. Bignell,<sup>2</sup> B. J. Coombes,<sup>2</sup> T. K. Eriksen,<sup>2</sup> T. J. Gray,<sup>2</sup> G. J. Lane,<sup>2</sup> and B. P. McCormick<sup>2</sup>

<sup>1</sup>*Research Center for Nuclear Physics (RCNP), Osaka University,  
10-1 Mihogaoka, Ibaraki, Osaka 567-0047, Japan*

<sup>2</sup>*Department of Nuclear Physics and Accelerator Applications, Research School of Physics,  
The Australian National University, Canberra, ACT 2601, Australia*

<sup>3</sup>*Department of Physics, GITAM Institute of Science,  
GITAM University, Visakhapatnam-530045, India*

<sup>4</sup>*Center for Nuclear Study, The University of Tokyo, Hongo, Bunkyo-ku, Tokyo 113-0033, Japan*  
<sup>5</sup>*Advanced Science Research Center, Japan Atomic Energy Agency, Tokai, Ibaraki 319-1195, Japan*

(Dated: May 16, 2022)

The electric monopole ( $E0$ ) transition strength  $\rho^2$  for the transition connecting the third  $0^+$  level, a “superdeformed” band head, to the “spherical”  $0^+$  ground state in doubly magic  $^{40}\text{Ca}$  has been determined via  $e^+e^-$  pair-conversion spectroscopy. The measured value,  $\rho^2(E0; 0_3^+ \rightarrow 0_1^+) = 2.3(5) \times 10^{-3}$ , is the smallest  $\rho^2(E0; 0^+ \rightarrow 0^+)$  found in  $A < 50$  nuclei. In contrast, the  $E0$  transition strength to the ground state observed from the second  $0^+$  state, a band head of “normal” deformation, is an order of magnitude larger,  $\rho^2(E0; 0_2^+ \rightarrow 0_1^+) = 25.9(16) \times 10^{-3}$ , which shows significant mixing between these two states. Large-Scale Shell Model (LSSM) calculations were performed to understand the microscopic structure of the excited states, and the configuration mixing between them; experimental  $\rho^2$  values in  $^{40}\text{Ca}$  and neighboring isotopes were well reproduced by the LSSM calculations. The unusually small  $\rho^2(E0; 0_3^+ \rightarrow 0_1^+)$  value is due to destructive interference in the mixing of shape-coexisting structures, which are based on several different multiparticle-multihole excitations. This observation goes beyond the usual treatment of  $E0$  strengths, where two-state shape mixing cannot result in destructive interference.

Shape coexistence is a unique feature of self-bound, finite, quantum many-body systems in which two or more different shapes emerge at similar excitation energies. This phenomenon is known to manifest in small atomic clusters [1] and molecules [2]. It also appears to be ubiquitous in atomic nuclei [3]. The shape of a nucleus is determined by the mean field generated by its constituent protons and neutrons. It is influenced by the number of nucleons, energy level density at the Fermi surface, an attractive residual interaction, and the principle that nuclear shapes may change to lower the energy of the system. A crucial difference between the atomic nucleus and more macroscopic systems is that quantum-mechanical tunnelling causes coexisting shapes to mix; each observed state is a superposition of configurations that correspond to the various shapes. In particular, shape coexistence occurs near closed-shell nuclei, where it is based on competition between the stabilizing effect of nucleon shell closures to retain a spherical shape, and the proton-neutron residual interaction which drives deformation via multiparticle-multihole excitations [3].

With the aid of modern radioactive-ion-beam facilities, shape coexistence has also been identified in nuclei far from the valley of  $\beta$  stability. This potentially affects locations of nuclear drip lines and waiting points that influence competition between  $\beta$  decay and neutron capture in cosmic nucleosynthesis. Experimental indications of shape coexistence have been reported in the double-closed-shell, neutron-rich nucleus  $^{78}\text{Ni}$  [4]. It can also be closely associated with the break down of familiar shell

structures, such as suppression of the  $N = 20$  shell gap in neutron-rich  $^{32}\text{Mg}$  [5, 6]. The  $0^+$  ground state, with very large quadrupole deformation parameter  $\beta_2 \approx 0.6$ , is supposed to coexist with a near-spherical first-excited  $0^+$  level [7]. Shape coexistence is generally discussed in terms of a two-state mixing model [3]. However, a two-state analysis of  $^{32}\text{Mg}$  questioned the aforementioned interpretation of a deformed ground state and spherical excited state [8, 9]. If three-level mixing is applied in  $^{32}\text{Mg}$  [10, 11],  $B(E2)$  values, level energies, and transfer cross sections can be successfully explained, but the  $0_3^+$  level in this nucleus has not been experimentally identified yet. More recently, the insufficiency of the two-state mixing model applied to the  $2^+$  states in  $^{42}\text{Ca}$  was also discussed [12].

Doubly magic  $^{40}\text{Ca}$  exhibits three distinct forms of quadrupole deformation: “spherical”, “normal deformation” (ND), and “superdeformation” (SD). Therefore, it provides a rare opportunity to study mixing effects between multiple configurations within a single nuclide. The first-excited,  $0_2^+$  state at 3.35 MeV is the head of a ND rotational band. The second-excited,  $0_3^+$  level at 5.21 MeV is the head of a SD band [13, 14]. In addition, the  $2_2^+$  level at 5.24 MeV is interpreted as a member of a  $K = 2$ , four-particle four-hole (4p-4h) band [15]. Emergence of various structures in low-lying levels in  $^{40}\text{Ca}$  indicates shape coexistence. The main configurations for the ND and SD structures are 4p-4h, and 8p-8h excitations across the  $N, Z = 20$  shell gap, respectively [15–20]. The transition quadrupole moments for the low-spin and

high-spin part of the SD band were reported to have a significant difference, indicating the mixing of lower-spin states with a less deformed configuration [14].

Furthermore, there is another unique feature of the SD band in  $^{40}\text{Ca}$ . Although SD nuclei are reported in several mass regions [21], SD band heads with  $J^\pi = 0^+$  are only observed in the  $A = 40$  [22, 23] and fission-isomer [21] regions. This makes it difficult to study their properties, such as mixing with less-deformed configurations, in detail. Therefore,  $^{40}\text{Ca}$  provides a unique testing ground in which the electric monopole ( $E0$ ) transition strength  $\rho^2(E0; 0^+ \rightarrow 0^+)$  between an SD band head and spherical ground state can be studied as a direct probe of shape mixing [25].

The  $\rho^2(E0; 0_3^+ \rightarrow 0_1^+)$  in  $^{40}\text{Ca}$  was previously investigated via the  $^{40}\text{Ca}(p,p')$  reaction by measuring  $e^+e^-$  pair decay with a plastic-scintillator pair spectrometer [27]. However, insufficient energy resolution meant that this state at 5.21 MeV was not resolved from the  $2_2^+$  state at 5.25 MeV, and an upper limit of  $\rho^2(E0; 0_3^+ \rightarrow 0_1^+) < 0.06$  was deduced. In order to accurately determine the value of  $\rho^2(E0; 0_3^+ \rightarrow 0_1^+)$  and understand the properties of the SD band, measuring the  $E0$  transition with higher energy resolution and low-background conditions is critical.

This Letter reports on a new study of excited states in  $^{40}\text{Ca}$  following proton inelastic scattering from a self-supporting, 1.5-mg/cm<sup>2</sup> thick, natural Ca target. Proton beams were delivered by the 14UD Pelletron tandem accelerator of the Heavy Ion Accelerator Facility at the Australian National University. The optimum beam energy to populate the  $0_3^+$  state, 8.6 MeV, was determined by scanning the beam energy and comparing relative yields of the 1.308-MeV,  $0_3^+ \rightarrow 2_1^+$  and 5.249-MeV,  $2_2^+ \rightarrow 0_1^+$   $\gamma$ -ray transitions.

Electron-positron ( $e^+e^-$ ) pair decays from excited states were measured by the superconducting solenoid, Super-e spectrometer [28–30]. The solenoid axis is perpendicular to the beam axis. The  $e^+e^-$  pairs emitted from the target are transported by the magnetic field to the Miel detector, an array of six 9-mm thick Si(Li) crystals. Two axial, Hevymet baffles are mounted between the target and detector to block  $\gamma$  rays and X rays, scattered beam particles, and secondary electrons. In this arrangement,  $e^+e^-$  pairs of nearly equal energy can reach the detector. The thickness of the segments allows for full absorption of pair decays formed from transition energies up to 8 MeV. The efficiency of the pair-conversion spectrometer was derived from Monte Carlo simulations that consider the magnetic field, energy, and angular correlation of emitted  $e^+e^-$  pairs. Spin alignment in the reaction and consequent angular distributions of  $e^+e^-$ -pair emission were taken into account [29].

A High-Purity Germanium (HPGe) detector was placed 1.5 m from the target and 135° relative to the beam axis to simultaneously detect  $\gamma$  rays emitted in the reactions. The relative  $\gamma$ -ray detection efficiency was measured using a  $^{56}\text{Co}$  source. Energies and detection times from the six Miel segments, energies from

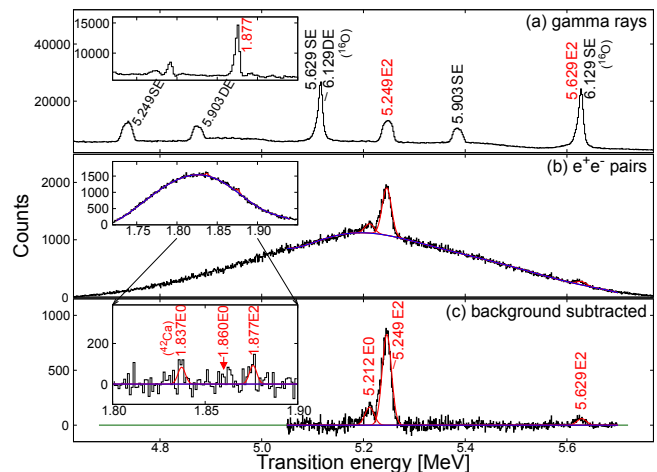


FIG. 1: (a) The  $\gamma$ -ray energy spectrum measured by the HPGe detector; (b)  $e^+e^-$  pair coincidence spectrum; (c) and  $e^+e^-$  spectrum after background subtraction. Peaks at 5.212, 5.249, and 5.629 MeV are labelled, as are single-escape (SE) and double-escape (DE) contaminant peaks.

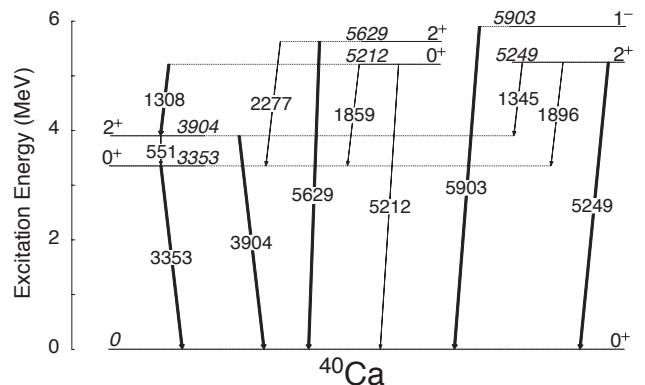


FIG. 2: Partial level scheme of  $^{40}\text{Ca}$  [31].

the HPGe detector, and the magnetic field values, were stored event-by-event and sorted offline.

The  $\gamma$ -ray and  $e^+e^-$  coincidence spectra analyzed to extract the  $\rho^2(E0)$  values are shown in Figure 1. Gamma-ray photo peaks, as well as single- and double-escape peaks associated with the 5.249- ( $2_2^+ \rightarrow 0_1^+$ ), 5.629- ( $2_3^+ \rightarrow 0_1^+$ ), and 5.903-MeV ( $1_1^- \rightarrow 0_1^+$ ) transitions of  $^{40}\text{Ca}$ , are evident. The half-lives of these states are  $83_{-9}^{+11}$ , 40(15), and 15.8(22) fs, respectively [31]. Since the stopping time of  $^{40}\text{Ca}$  recoils in the target is approximately 0.3 ps, these  $\gamma$  rays are emitted while the nucleus is in motion and the peaks are consequently Doppler broadened. The  $\gamma$ -ray energy spectrum corrected for Doppler shift is presented in Fig. 1(a). Escape peaks of the 6.129-MeV  $\gamma$  ray in  $^{16}\text{O}$  [32], from oxidation of the Ca target, are also visible. Since the half-life of this state is 18.4 ps, these  $\gamma$  rays are emitted after stopping and the associated peaks are sharp.

The  $e^+e^-$  pair spectrum is shown in Fig. 1(b) with the energy axis shifted by 1.022 MeV to correspond to the

TABLE I: Summary of  $\rho^2(E0; 0^+ \rightarrow 0^+)$  values in  $^{40}\text{Ca}$ .

Transition	Energy (MeV)	$\tau(E0)$ (ns)	$\Omega_\pi(E0)$ [33]	$\rho^2 \times 10^3$
$0_2^+ \rightarrow 0_1^+$	3.353	3.13(12)	$1.24(6) \times 10^{10}$	25.9(16)
$0_3^+ \rightarrow 0_1^+$	5.212	3.2(7)	$1.36(7) \times 10^{11}$	2.3(5)
$0_3^+ \rightarrow 0_2^+$	1.859	>76	$2.79(14) \times 10^8$	<45

associated transition energies. A background that was parametrized by a polynomial function was subtracted, giving the  $e^+e^-$  pair spectrum presented in Fig. 1(c). There is a peak at 5.212 MeV with no associated  $\gamma$  ray; this is the  $E0, 0_3^+ \rightarrow 0_1^+$  transition. The only other peaks observed in panels (b) and (c) are the 5.249- and 5.629-MeV,  $E2$  transitions from the  $2_2^+$  and  $2_3^+$  levels to the ground state.

Extraction of  $\rho^2$  values was based on analysis of  $\gamma$ -ray and  $e^+e^-$  spectral yields. The term  $\rho^2$  is related to the measured  $E0$  transition rate,  $1/\tau(E0)$ , by [25]:

$$\frac{1}{\tau(E0)} = \rho^2(\Omega_K + \Omega_{L_1} + \dots + \Omega_\pi), \quad (1)$$

where the  $\Omega_j$  terms are electronic factors associated with atomic shells ( $K, L_1, \dots$ ). For both electron and  $e^+e^-$  pair conversion ( $\pi$ ) they depend on the atomic number and transition energy; numerical evaluations are available [33, 34]. The electron conversion contributions to the  $E0$  transitions considered here are <0.6% ( $0_2^+ \rightarrow 0_1^+$  and  $0_3^+ \rightarrow 0_1^+$ ) and 11% ( $0_3^+ \rightarrow 0_2^+$ ). The relevant values of  $\Omega_\pi$  are included in Table I.

The mean lifetime of the  $0_3^+$  state,  $\tau = 1.47(30)$  ps, is known from Doppler-shift attenuation measurements [35]. Figure 2 shows the partial level scheme of  $^{40}\text{Ca}$  relevant to the present analysis [31]; the  $0_3^+$  state decays by a 1.308-MeV,  $E2$   $\gamma$ -ray transition, or by 1.859- or 5.212-MeV,  $E0$  transitions. While the 1.859-MeV,  $0_3^+ \rightarrow 0_2^+$   $E0$  component was sought by optimizing the Super-e magnetic field for that transition energy, a clear peak was not observed above background (see Fig. 1(c)); however, an upper limit was established for the branching ratio. Therefore, using the measured  $\gamma$ -ray and  $e^+e^-$  pair intensities and theoretical pair conversion coefficients from BrIcc [34], all decay branches from the  $0_3^+$  state were determined. A value of  $\rho^2(E0; 0_3^+ \rightarrow 0_1^+) = 2.3(5) \times 10^{-3}$  was extracted. An upper-limit of  $\rho^2(E0; 0_3^+ \rightarrow 0_2^+) < 4.5 \times 10^{-2}$  was also obtained for the 1.859-MeV transition. The significantly smaller value of  $\Omega_\pi(E0)$  explains why this transition was not observed directly in the experiment.

Since the  $0_2^+$  level is the lowest excited state and, consequently, has a single  $E0$  decay branch to the ground state, evaluation of  $\rho^2(E0; 0_2^+ \rightarrow 0_1^+) = 25.9(16) \times 10^{-3}$  from the known lifetime was less complex. This  $\rho^2$  value

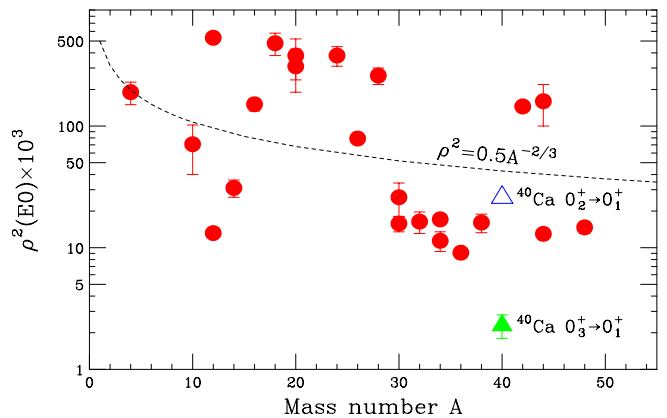


FIG. 3: Systematics of  $\rho^2(E0; 0^+ \rightarrow 0_1^+)$  values of even-even,  $A < 50$  nuclei (filled circles) [36]. The  $\rho^2(E0; 0_3^+ \rightarrow 0_1^+)$  in  $^{40}\text{Ca}$  from this work are shown as open and filled triangles.

is large, indicating significant shape differences and mixing between the two states. The  $E0$  transition strengths from our work are summarized in Table I. Systematic behavior of  $\rho^2(E0; 0^+ \rightarrow 0_1^+)$  values for even-even nuclei with  $A < 50$  [36] is presented in Figure 3. The dashed line corresponds to  $\rho^2(E0) = 0.5A^{-2/3}$  [25]. The  $\rho^2(E0; 0_2^+ \rightarrow 0_1^+)$  value measured in the present work shows good agreement with the systematic trend. Conversely,  $\rho^2(E0; 0_3^+ \rightarrow 0_1^+)$  is significantly smaller than the trendline, and all of the other experimental values.

In general, the  $E0$  transition strength between states in a nucleus gives a direct measure of shape mixing between them [24]. The associated mixing amplitude  $\alpha$  is usually estimated by considering a simple two-state model with spherical and deformed wave functions [25]. In such a case,  $\rho^2(E0)$  is related to  $\alpha$  and the difference in square of quadrupole deformation parameters,  $\Delta(\beta_2^2)$ , by:

$$\rho^2(E0) = \left(\frac{3}{4\pi}Z\right)^2 \alpha^2(1 - \alpha^2) [\Delta(\beta_2^2)]^2. \quad (2)$$

Using the measured  $\rho^2(E0)$  and the reported  $\beta_2$  values of  $0.27(5)$  and  $0.59_{-0.07}^{+0.11}$  for the  $0_2^+$  and  $0_3^+$  states, respectively [13],  $\alpha_{2 \rightarrow 1} = 0.55(37)$  and  $\alpha_{3 \rightarrow 1} = 2.9_{-0.8}^{+1.1} \times 10^{-2}$  were determined for the  $0_2^+ \rightarrow 0_1^+$  and  $0_3^+ \rightarrow 0_1^+$  transitions. Here, the  $\beta_2(0_1^+) = 0$  [26] was assumed. Within the two-state model, the small mixing for the  $0_3^+ \rightarrow 0_1^+$  transition implies a very small overlap of wave functions between the spherical ground state and SD band head.

Large-Scale Shell-Model (LSSM) calculations were performed to gain a microscopic understanding of the measured  $\rho^2(E0)$  values and the structure of  $^{40}\text{Ca}$ . Assuming an inert  $^{16}\text{O}$  core, the valence model space included the full  $sd$  shell ( $0d_{5/2}, 1s_{1/2}, 0d_{3/2}$ ) and restricted  $fp$  shell ( $0f_{7/2}, 1p_{3/2}$ ) orbitals. The calculations used  $E0$  effective charges of  $(e_p, e_n) = (1.8, 0.8)e$ , and harmonic-oscillator (HO) single-particle wave functions with  $\hbar\omega = 45A^{-1/3} - 25A^{-2/3}$  MeV.

TABLE II: Calculated excitation energies and  $mp$ - $mh$  probabilities of the  $0_{1,2,3}^+$  states in  $^{40}\text{Ca}$ .

$E_x$ (MeV)	$0p$ - $0h$	$2p$ - $2h$	$4p$ - $4h$	$6p$ - $6h$	$8p$ - $8h$	$10p$ - $10h$
$0_1^+$	0	0.46	0.39	0.13	0.02	0.00
$0_2^+$	2.81	0.04	0.03	0.63	0.26	0.03
$0_3^+$	6.37	0.02	0.07	0.11	0.23	0.56

The effective interaction was designed to describe multiparticle-multihole ( $mp$ - $mh$ ) excitations across the  $N = Z = 20$  shell gap by tuning the SDPF-M interaction [37, 38] within the model space, which was truncated to include  $m \leq 10$ . The tuning was carried out so that one-neutron separation energies of  $^{40,41}\text{Ca}$  and one- $\alpha$  separation energies of  $^{40}\text{Ca}$  and  $^{44}\text{Ti}$  were reproduced with the many-body correlations that were included. Recently, this interaction was successfully applied to high-spin states in  $^{35}\text{S}$  [39].

Calculated  $mp$ - $mh$  probabilities for  $0_{1,2,3}^+$  states of  $^{40}\text{Ca}$  are listed in Table II. The dominance of  $m = 0, 4, 8$  configurations in  $0_{1,2,3}^+$  is clearly observed; this structure is consistent with Ref. [20]. There is also considerable mixing, especially with neighboring values of  $m$ .

Figure 4 shows  $\rho^2(E0)$  values for  $A \approx 40$  nuclei whose excited  $0^+$  states are dominated by  $mp$ - $mh$  excitations. Data for  $^{36}\text{S}$ ,  $^{38}\text{Ar}$ ,  $^{42}\text{Ca}$  [36, 40] and  $^{40}\text{Ca}$  (this work) are plotted with the corresponding LSSM calculations. Overall, the theory reproduces the experimental data fairly well; in particular, excellent agreement was found for the  $0_3^+ \rightarrow 0_1^+$  in  $^{40}\text{Ca}$  despite its value being lowest among the  $Z < 50$  nuclei. The upper limit value for the  $0_3^+ \rightarrow 0_2^+$  transition is also consistent with the LSSM result.

All of the ground states considered in Fig. 4 are near spherical, whereas the  $0_2^+$  states in  $^{36}\text{S}$ ,  $^{38}\text{Ar}$  and  $^{40}\text{Ca}$  are considered to have normal deformations [41]. With similar  $\rho^2(E0) \times 10^3 \approx 10$  to 20 values, these  $0_2^+ \rightarrow 0_1^+$  transitions are in accordance with the two-state analysis of Eq. (2) when similar mixing amplitudes are employed. However, the  $0_2^+$  state in  $^{42}\text{Ca}$  [42] and the  $0_3^+$  state in  $^{40}\text{Ca}$  [13] are strongly deformed, yet their  $\rho^2$  values for the transition to the ground state are completely different. This unexpected observation stimulates a detailed analysis of the role of mixing, which is described below.

In the present calculation, HO wave functions were used in a model space that prohibited single-nucleon excitations of  $2\hbar\omega$ , such as  $0s \rightarrow 1s0d$ . A many-body state,  $|\Psi_i\rangle$ , may be decomposed into its  $mp$ - $mh$  components,  $|\Psi_i\rangle = \sum_m |\Psi_i(m)\rangle$ , such that:

$$\langle \Psi_f | r^2 | \Psi_i \rangle = b^2 \sum_m w(m) \xi_{if}(m), \quad (3)$$

where  $b = \sqrt{\hbar/(M\omega)}$  is the HO length parameter,  $w(m) = m + c(^{40}\text{Ca})$  are the weighting fac-

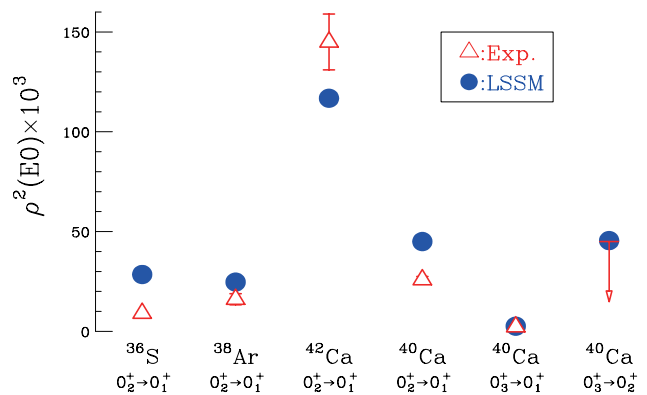


FIG. 4: Systematics of  $\rho^2(E0)$  values for  $^{36}\text{S}$ ,  $^{38}\text{Ar}$ ,  $^{42}\text{Ca}$  and  $^{40}\text{Ca}$ . Open triangles are experimental values from Refs. [36, 40] and this work; filled circles are LSSM calculations.

tors for each value of  $m$  with  $c(^{40}\text{Ca}) = 120$ , and  $\xi_{if}(m) = \langle \Psi_f(m) | \Psi_i(m) \rangle$  are the overlap factors between initial and final states, denoted  $i$  and  $f$ , with  $0^+$  assignments are considered. For  $f \neq i$ ,  $\sum_m \xi_{if}(m) = 0$  must also be satisfied from the imposed orthogonality condition,  $\langle \Psi_f | \Psi_i \rangle = \delta_{if}$ .

Since  $N = Z = 20$  in  $^{40}\text{Ca}$ ,  $T = 0$  for all  $0^+$  states and only isoscalar transitions contribute. Hence, the  $E0$  matrix element is given by:

$$\begin{aligned} M(E0; i \rightarrow f) &= \sum_m M_{if}(m), \\ &= e_{\text{IS}} \times b^2 \cdot \sum_m (w(m) \cdot \xi_{if}(m)), \end{aligned} \quad (4)$$

where  $e_{\text{IS}} = (e_p + e_n)/2$ . The individual  $M_{if}(m)$  terms are, therefore, described by a weight factor  $w(m)$  and an overlap factor  $\xi_{if}(m)$ .

In Figure 5,  $\xi_{if}(m)$  and  $M_{if}(m)$  are plotted for each contributing value of  $m$ . The orthogonality condition also allows the weighting factors to be adjusted without affecting the total  $E0$  matrix element. In this case, the large values of  $w(m)$  for  $^{40}\text{Ca}$  ( $m + 120$ ) may be replaced with a smaller value,  $w(m') = m - \bar{m}$ , where  $\bar{m} = \sum_m m \times \xi(m)^2 / \sum_m \xi(m)^2$  for each transition. The total  $E0$  strength is independent of the choice of  $\bar{m}$ , but such a shift reduces the amplitude of each  $M_{if}(m)$  value, thus facilitating the understanding of how the individual mixing amplitudes contribute to the total  $E0$  matrix element. The  $M_{if}(m)$  values shown in Fig. 5(b) were determined with the scaled weighting factors,  $w(m')$ .

Figure 5(a) shows that both the  $0_2^+ \rightarrow 0_1^+$  and  $0_3^+ \rightarrow 0_2^+$  transitions have negative  $\xi_{if}(m)$  values for small  $m$  that change sign once and become positive at larger  $m$ . In such cases,  $w(m')$  may be chosen so that the  $M_{if}(m)$  values add constructively, as presented in Fig. 5(b), and

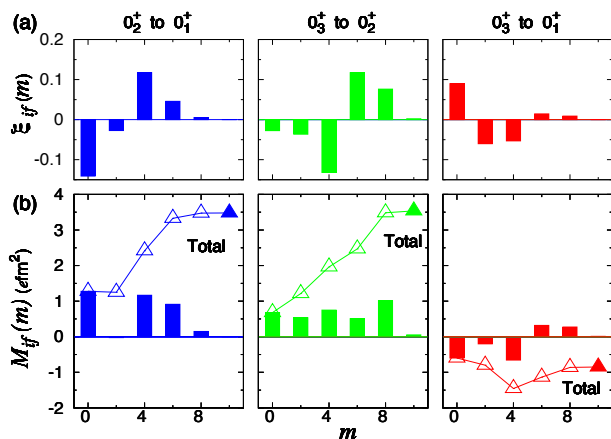


FIG. 5: (a) Overlap  $\xi_{if}(m)$  and (b)  $E0$  matrix element  $M_{if}(m)$  for each  $m$  value of the  $mp$ - $mh$  excitation. The summed  $E0$  matrix elements  $\sum_{m' < m} M_{if}(m')$  and the total values are shown by the open and filled triangles, respectively.

the resulting  $E0$  matrix element is moderate. On the other hand, the  $0_3^+ \rightarrow 0_1^+$  transition is rather different: the  $\xi_{if}(m)$  values change sign twice at  $m = 0 \rightarrow 2$  and  $m = 4 \rightarrow 6$ . In this case, destructive interference of  $M_{if}(m)$  is inevitable for any possible value of  $w(m')$ .

Finally, the two-state description is revisited in terms of the present microscopic analysis. A system obeying this model should have two non-vanishing  $\xi_{if}(m)$  values at  $m = m_1, m_2$  constrained to  $\xi_{if}(m_1) + \xi_{if}(m_2) = 0$ . This system has only one degree of freedom, corresponding to  $\alpha$  in Eq. (2); no phase factor is relevant to the observables. In contrast, when three states are involved there are two degrees of freedom, and interference occurs between them. The very small  $\rho^2(E0; 0_3^+ \rightarrow 0_1^+)$  value is a manifestation of this new aspect of shape coexistence with three-state mixing.

Note that the degree of the mixing between SD and ND can be probed with  $B(E2; 0_3^+ \rightarrow 2_1^+)$ . The calculated value, 1.3 W.u., is significantly smaller than the measured value,  $17_{-3}^{+4}$  W.u. Considering the moderate  $\rho(E0; 0_3^+ \rightarrow$

$0_2^+)$  value by LSSM (see Fig. 3), we do not expect larger mixing between those bands. This underestimate may be due to incorrect  $K$  mixing between the  $2_1^+$  and  $2_2^+$  states.

In summary, the  $E0$  transition strength of  $\rho^2(E0; 0_3^+ \rightarrow 0_1^+) = 2.3(5) \times 10^{-3}$  was measured for the first time in doubly magic  $^{40}\text{Ca}$ ; this is the lowest  $\rho^2(E0)$  value measured among nuclei of  $A < 50$ . An upper limit of  $\rho^2(E0; 0_3^+ \rightarrow 0_2^+) < 4.5 \times 10^{-2}$  was also obtained. Large-scale shell-model calculations were performed for  $^{40}\text{Ca}$  and several neighboring nuclei. The calculated  $E0$  matrix elements were analyzed in terms of multiparticle-multipole configuration mixing. Moderately large  $\rho^2(E0)$  values for the  $0_2^+ \rightarrow 0_1^+$  and  $0_3^+ \rightarrow 0_2^+$  transitions are consistent with a two-state model, in which only a squared mixing amplitude matters. Conversely, the extremely small  $\rho^2(E0; 0_3^+ \rightarrow 0_1^+)$  value is caused by destructive interference among  $mp$ - $mh$  components in a three-state mixing scenario. The new data and shell-model calculations provide a novel perspective on multiple shape coexistence, with implications for experimental and theoretical activities extending to nuclei far from stability.

This work is supported by the International Joint Research Promotion Program of Osaka University, JSPS KAKENHI Grant Number JP 17H02893, 18H03703, JSPS A3 Foresight program Grand Number JPJSA3F20190002, and the Australian Research Council grant numbers DP140102896 and DP170101673. N. S. and Y. U. acknowledge KAKENHI grants (20K03981, 17K05433), “Priority Issue on post-K computer” (hp190160, hp180179, hp170230) and “Program for Promoting Researches on the Supercomputer Fugaku” (hp200130, hp210165), MEXT, Japan. E.I., N.A., N.S., and Y.U. acknowledge support from the RCNP Collaboration Research Network (RCNP COREnet); A.A., B.J.C., J.T.H.D., T.J.G., and B.P.M. acknowledge support of the Australian Government Research Training Program. Support for the ANU Heavy Ion Accelerator Facility operations through the Australian National Collaborative Research Infrastructure Strategy (NCRIS) program is also acknowledged. The authors thank J. Heighway for preparing targets. E.I. acknowledges fruitful discussions with J.L. Wood on issues of shape coexistence.

- 
- [1] M. Horoi and K. A. Jackson, Chem. Phys. Lett. **427**, 147 (2016) and references therein.
- [2] “Molecular Structure” Chemistry Foundations and Applications. Volume 3. Farmington, MI: J.J. Lagowski, 2004.
- [3] K. Heyde and J. L. Wood, Rev. Mod. Phys. **83**, 1467 (2011).
- [4] R. Taniuchi, *et al.*, Nature **569**, 53 (2019).
- [5] D. Guilemaud-Mueller, *et al.*, Nucl. Phys. A **426**, 37 (1984).
- [6] T. Motobayashi, *et al.*, Phys. Lett. B **346**, 9 (1995).
- [7] K. Wimmer, T. Kröll, R. Krücken, V. Bildstein, R. Gernhäuser, B. Bastin, *et al.*, Phys. Rev. Lett. **105**, 252501 (2010).
- [8] H. T. Fortune, Phys. Rev. C **84**, 024327 (2011).
- [9] H. T. Fortune, Phys. Rev. C **85**, 014315 (2012).
- [10] A. O. Macchiavelli, H.L. Crawford, C.M. Campbell, R.M. Clark, M. Cromaz, P. Fallon, *et al.*, Phys. Rev. C **94**, 051303(R) (2016).
- [11] A. O. Macchiavelli and H. L. Crawford, Phys. Scr. **92**, 064001 (2017).
- [12] K. Hadyńska-Kleń, *et al.*, Phys. Rev. C **97**, 024326

- (2018).
- [13] E. Ideguchi, D.G. Sarantites, W. Reviol, A.V. Afanasjev, M. Devlin, C. Baktash, *et al.*, Phys. Rev. Lett. **87**, 222501 (2001).
- [14] C.J. Chiara, E. Ideguchi, M. Devlin, D.R. LaFosse, F. Lerma, W. Reviol, S.K. Ryu, D.G. Sarantites, *et al.*, Phys. Rev. C **67**, 041303(R) (2003).
- [15] W. J. Gerace and A. M. Green, Nucl. Phys. A **123**, 241 (1969).
- [16] H.T. Fortune, M.N.I. Al-Jadir, R.R. Betts, J.N. Bishop, R. Middleton, Phys. Rev. C **19**, 756 (1979).
- [17] R. Middleton, J. Garrett, H.T. Fortune, Phys. Lett. B **39**, 339 (1972).
- [18] W. Bohne, K.D. Buchs, H. Fuchs, *t al.*, Nucl. Phys. A **284**, 14 (1977).
- [19] W.J. Gerace and A.M. Green, Nucl. Phys. A **93**, 110 (1967).
- [20] E. Caurier, J. Menéndez, F. Nowacki, A. Poves, Phys. Rev. C **75**, 054317 (2007).
- [21] B. Singh, R. Zywina, R. B. Firestone, Nucl. Data Sheets **97**, 241 (2002).
- [22] C. E. Svensson, A.O. Macchiavelli, A. Juodagalvis, A. Poves, I. Ragnarsson, S. Åberg, *et al.*, Phys. Rev. Lett. **85**, 2693 (2000).
- [23] E. Ideguchi, *et al.*, Phys. Lett. B **686**, 18 (2010).
- [24] A.V. Aldushchenkov and N.A. Voinova, Nucl. Data Tables **11**, 299 (1972).
- [25] J. L. Wood *et al.*, Nucl. Phys. A **651**, 323 (1999).
- [26] R. F. Garcia Ruiz, *et al.*, Nature Phys. **12**, 594 (2016).
- [27] M. Ulrickson, *et al.*, Phys. Rev. C **15**, 186 (1977).
- [28] T. Kibédi, G. D. Dracoulis and A. P. Byrne, Nucl. Instrum. Meth. A **294**, 523 (1990).
- [29] T. K. Eriksen, T. Kibédi, M.W. Reed, A.E. Stuchbery, K.J. Cook, A. Akber, *et al.*, Phys. Rev. C **102**, 024320 (2020).
- [30] J. T. H. Dowie, *et al.*, Phys. Lett. B **811**, 135855 (2020). Nucl. Phys. A **131**, 113 (1969).
- [31] J. Chen, Nucl. Data Sheets **140**, 1 (2017).
- [32] D. R. Tilley, H. R. Weller, and C. M. Cheves, Nucl. Phys. A **564**, 1 (1993).
- [33] J. T. H. Dowie, *et al.*, At. Data Nucl. Data **131**, 101283 (2020).
- [34] T. Kibédi, *et al.*, Nucl. Instrum. Meth. A **589**, 202 (2008).
- [35] A. R. Poletti, *et al.*, Phys. Rev. **181**, 1606 (1969).
- [36] T. Kibédi, A.B. Garnsworthy, and J.L. Wood, Prog. Part. and Nucl. Phys. **123**, 103930 (2022)
- [37] Y. Utsuno, T. Otsuka, T. Mizusaki and M. Honma, Phys. Rev. C **60**, 054315 (1999).
- [38] Y. Utsuno, T. Otsuka, T. Glasmacher, T. Mizusaki, M. Honma, Phys. Rev. C **70**, 044307 (2004).
- [39] S. Go, E. Ideguchi, R. Yokoyama, N. Aoi, F. Azaiez, K. Furutaka, *et al.*, Phys. Rev. C **103**, 034327 (2021).
- [40] J. W. Olness, W. R. Harris, A. Gallmann, *et al.*, Phys. Rev. C **3**, 2323 (1971).
- [41] J. L. Wood, *et al.*, Phys. Rep. **215**, 101 (1992).
- [42] K. Hadyńska-Klęk, *et al.*, Phys. Rev. Lett. **117**, 062501 (2016).